Escape from end-pinching in Herschel-Bulkley ligaments

Shu Yang, Fahim Tanfeez Mahmood, C. Ricardo Constante-Amores*

Department of Mechanical Science and Engineering,

University of Illinois Urbana-Champaign

Abstract

Capillary retraction of Herschel-Bulkley ligaments displays a rich set of behaviours that depart significantly from the classical Newtonian picture. We focus here on the low-viscosity regime, where droplet detachment is controlled by the end-pinching mechanism. Using fully resolved axisymmetric simulations, we show that viscoplasticity and shear-dependent rheology reorganize the fundamental routes by which a retracting ligament may pinch off or escape breakup. Four dynamical outcomes are identified: inertial pinch-off, viscous escape driven by an attached vorticity layer, inertial escape caused by vortex-ring detachment, and complete arrest when yielding suppresses motion. These regimes appear in an orderly structure across the rheological parameter space, but their transitions are governed by a single unifying feature of the neck dynamics: whether inertia, viscous diffusion, or yield stress dominates the local collapse. When inertia dominates, the vorticity sheet detaches and rolls into a vortex ring, producing an inertial rebound of the neck. When viscous effects dominate, the vorticity layer remains attached and drives a back-flow that reopens the neck. When yield stress is sufficiently large, both mechanisms are suppressed and the ligament becomes motionless. This framework extends the Newtonian end-pinching and escape mechanisms to viscoplastic fluids and clarifies how non-Newtonian rheology reshapes capillary-driven retraction.

I. INTRODUCTION

Capillary-driven ligament retraction is a canonical problem in free-surface flows, with relevance to both natural and industrial processes involving liquid fragmentation and droplet formation [1–3]. Such dynamics underpin the formation of natural sprays and jets, and are central to technologies including drop-on-demand inkjet printing, spray coating, catalyst manufacture, and agricultural spraying [4–11].

For cylindrical Newtonian ligaments, the retraction is dominated by a competition between capillary forces and viscosity. For cases with sufficiently low viscosity (nearly inviscid), the capillary retraction results in the formation of a bulbous structure at the ligament tip which thins to result in droplet detachment. This is known as the classical end-pinching mechanism [1, 12]. Hoepffner and Paré [13] showed that viscosity could suppress the pinch-off, allowing the ligament to escape end-pinching altogether, in which increasing viscosity leads

^{*} crconsta@illinois.edu

to the formation and eventual detachment of a vortex ring generated by backflow through the neck. This detachment reorganizes the local pressure field, drives fluid back toward the neck, and reopens it, thereby preventing breakup.

Beyond the Newtonian dynamics described above, ligament retraction becomes considerably richer when interfacial or bulk rheology is altered. In particular, surfactants and non-Newtonian constitutive behaviour introduce new stress mechanisms that can either enhance or suppress end-pinching [14–17] Surfactant-laden ligaments can produce strong Marangoni stresses as surface tension gradients develop, leading to modified vorticity generation at the retracting tip. Even in inviscid limits, these interfacial stresses are sufficient to reverse the classical end-pinching scenario and drive end-pinching escape, as demonstrated by Constante-Amores et al. [14]. In a related configuration, Deka et al. [18] investigated the retraction of Bingham liquid sheets in two dimensions and reported qualitatively different outcomes depending on the relative strength of viscous stresses. Their study identified two principal regimes—complete retraction and no retraction—demonstrating how yield stress can suppress capillary-driven motion. This dependence arises because increasing viscous stresses reduce the local strain rates and thereby the total stress available to exceed the yield threshold, which both enlarges unyielded regions and ultimately prevents capillary forces from driving retraction.

As shown above, the retraction of non-Newtonian ligaments, in the limit of low viscosity, remains far less understood than its Newtonian counterpart, with only limited studies addressing how yield stress and shear-dependent viscosity alter end-pinching dynamics for other geometries (i.e., sheet retraction). In this work, we focus specifically on the axisymmetric retraction of Herschel–Bulkley ligament in air, where the combined effects of finite yield stress and shear-rate-dependent mobility modify the balance between capillary forces and viscous dissipation. Using direct numerical simulations and theory, we characterize how these rheological features reshape neck formation, tip dynamics, and the pathways leading to pinch-off or complete escape from the capillary singularity. The paper is organized as follows: section II presents the numerical method and key parameter calculations. Section III presents the influence of yield-stress and shear-rate dependent effects on the dynamics. Finally, we present the key findings in section IV and propose future research directions.

II. NUMERICAL SIMULATIONS

The two-phase Navier-Stokes equations were solved using the one-fluid formulation in the open-source software Basilisk [19, 20]. Distances, times and pressures are made non-dimensional using as characteristic values: ligament radius R_0 , $(\rho R_0^3/\sigma)^{1/2}$ and σ/R_0 , where ρ represents liquid density, and σ denotes surface tension. Therefore, velocities are non-dimensionalized using Taylor-Culick velocity $(\sigma/\rho R_0)^{1/2}$.

Applying this scaling yields the dimensionless equations

$$\nabla \cdot \boldsymbol{u} = 0, \quad \frac{\partial \boldsymbol{u}}{\partial t} + \boldsymbol{u} \cdot \nabla \boldsymbol{u} = -\nabla p + \nabla \cdot \boldsymbol{\tau} + \kappa \mathbf{n} \delta_s, \tag{1}$$

here, u is the velocity field and p is the pressure, τ is the deviatoric stress tensor. κ , \mathbf{n} , and δ_s denote the interface curvature, unit normal vector to the interface, and surface delta function.

The ligament is modeled as a Herschel-Bulkley fluid, excluding effects of elastic storage, memory, and polymeric stretching. The deviatoric stress, and the stress tensor for this fluid is expressed as:

$$\tau = 2 \left[\frac{\tau_y}{2\|\mathcal{D}\| + \varepsilon} \mathcal{I} + K(2\|\mathcal{D}\| + \varepsilon)^{n-1} \right] \mathcal{D}$$
 (2)

where $\|\mathcal{D}\|$ is the second invariant of the deformation rate tensor, τ_y denotes liquid yield stress, and K represents consistency index.

The dimensionless numbers controlling the equations above are the plastocapillary number (\mathcal{J}) , which accounts for the competition between capillary and yield stresses, the Ohnesorge number (Oh_K) , which compares inertial-capillary to inertial-viscous timescales, n is the flow-behaviour index, which determines the shear-rate dependence of the apparent viscosity, m is the normalized viscosity ratio, and ρ_r is the density ratio, ligament to external phase. Here, μ_{ext} and ρ_{ext} denotes external phase viscosity and density, respectively, and $\dot{\gamma}_c$ is characteristic shear rate. These dimensionless numbers are defined as

$$\mathcal{J} = \frac{\tau_y R_0}{\sigma}, Oh_K = \frac{K\dot{\gamma}_c^{n-1}}{\sqrt{\rho\sigma R_0}}, m = \frac{K\dot{\gamma}_c^{n-1}}{\mu_{\text{ext}}}, \rho_r = \frac{\rho}{\rho_{\text{ext}}}$$
(3)

The initial numerical setup closely follows the work of Notz and Basaran [12]. We consider a viscoplastic ligament of initial radius R_0 surrounded by air. The Herschel-Bulkley constitutive law is implemented via a regularized formulation, in which the apparent viscosity is smoothed through an ε -dependent function to avoid singularities as $\|\mathcal{D}\| \to 0$, where

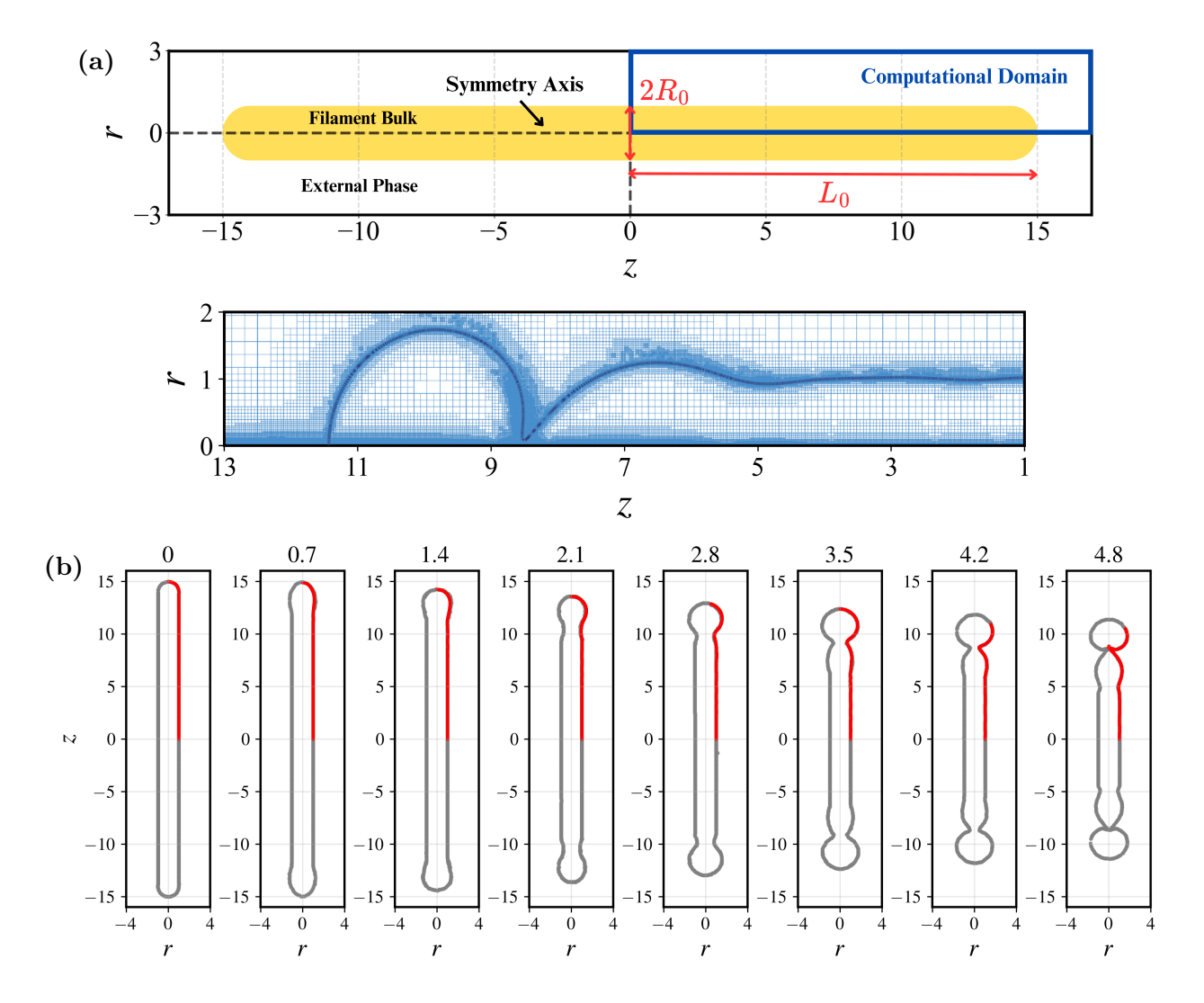


FIG. 1: (a) Schematic of the initial configuration of the system (top panel) and the computational mesh used in the simulations (bottom panel). (b) Spatio-temporal evolution of a retracting ligament for $L_o = 15, Oh_K = 0.001, \mathcal{J} = 0$ (Newtonian). The red lines correspond to the results of the present study and the solid black lines are collected from Notz and Basaran [12].

 \mathcal{D} denotes the rate-of-deformation tensor. As a result, the yield surface cannot be sharply resolved, since $\|\mathcal{D}\|$ remains strictly positive for any finite $\varepsilon > 0$. Nevertheless, regions where $\|\mathcal{D}\|$ falls below a prescribed threshold can be interpreted as approximately unyielded. ε dependence is examined in appendix IV for the base configuration.

The motionless ligament is initialized as a cylindrical ligament of aspect ratio $\mathcal{L} = L_0/R_0 = 15$ and hemispherical caps at its ends (see figure 1a), as in previous work by Notz and Basaran [12]. The computational domain spans 25×25 , with the ligament ini-

tially occupying the axial range from 0 to 15. At the outer radial boundary, we impose a zero normal pressure gradient (Neumann). Along the axis of symmetry, axisymmetric regularity is enforced by setting $u_r = 0$, $u_\theta = 0$, and $\partial p/\partial r = 0$. We use an adaptive mesh refinement (AMR) strategy based on wavelet-estimated discretization error [21], and a similar mesh refinement and neck interface tracking strategies to capture pinch-off adopted by Yang et al. [22]. A mesh study was carefully done for this setup, and a max level of 12 was selected. We note that our resolution is higher than previous viscoplastic sheet retraction from Deka et al. [18] (2¹⁰), as we are aiming to capture the interfacial singularity. Velocity and other temporal fields are solved through Basilisk using a classical time-splitting projection method [19].

Figure 1b compares our numerical predictions with the results of Notz and Basaran [12] and shows excellent agreement in the spatio-temporal evolution of the interface shape. We restrict our attention to the primary retraction dynamics and the neck evolution, and do not consider subsequent secondary breakup processes. When breakup does not occur, we continue the simulations only until the viscoplastic droplet fully forms, limiting the total integration time to less than 10 non-dimensional units. The simulation is initialized with fluids at rest in the absence of gravity.

III. RESULTS

The interplay between capillarity, rheology, and inertia gives rise to four distinct dynamical pathways—pinch-off, viscous escape, inertial rebound, and arrested motion. Their organization in the (n, \mathcal{J}) plane is governed by the evolving local Ohnesorge number $Oh_{loc}(t) = \mu_{eff}(t)/\sqrt{\rho\sigma r_{min}(t)}$, evaluated at the neck. This dimensionless quantity characterizes the instantaneous competition between viscous, capillary, and inertial stresses, and thus provides a direct measure of the local flow regime during thinning.

A. Phenomenological regime map in n and \mathcal{J} space

We begin the discussion of the results by presenting a phenomenological regime map in the (n, \mathcal{J}) parameter space at $Oh_K = 0.001$ and L = 15. Figure 2 illustrates the distinct outcomes and their corresponding boundaries. Approximately 100 simulations were

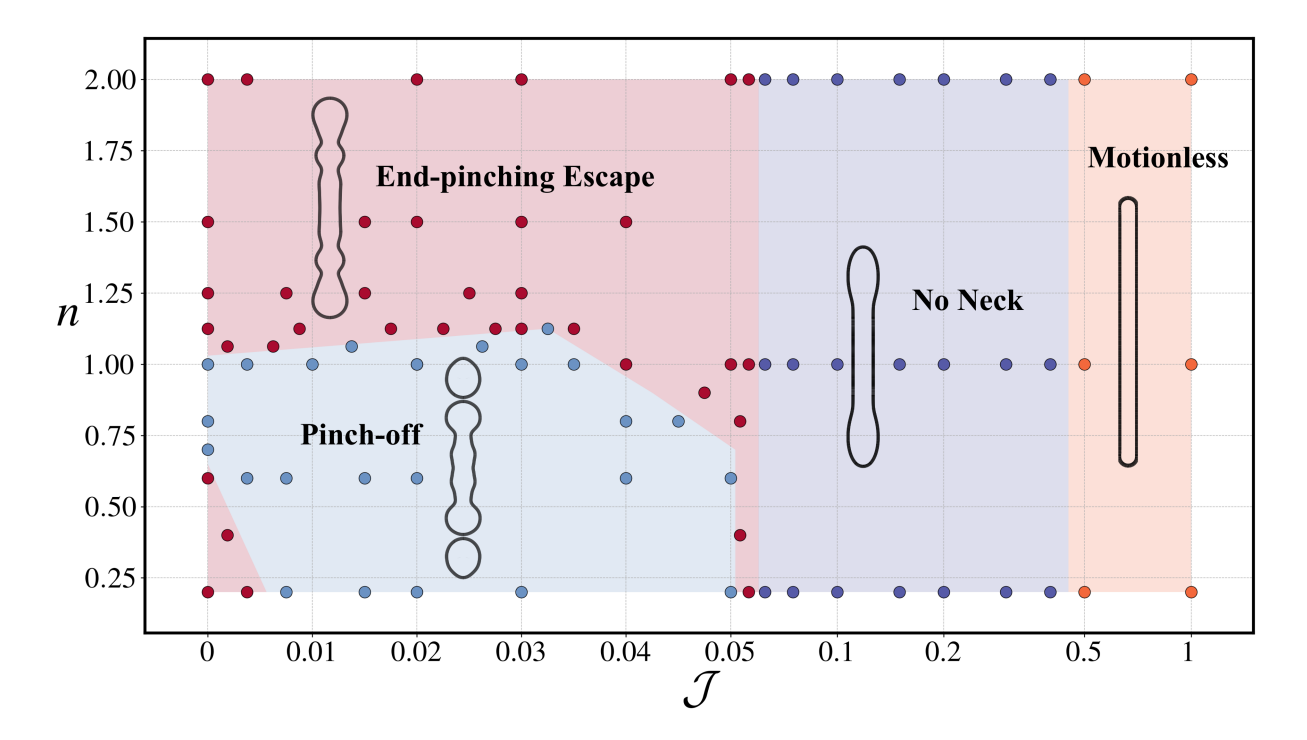


FIG. 2: Regime map in terms of the plastocapillary number \mathcal{J} and the flow index parameter n for $Oh_K = 0.001$ showing the transitions between the different categories identified in the current study. The insets show a representative case from each of the four regimes. The symbols represent simulations at the different transition lines.

performed to delineate these boundaries accurately. Each point on the map was classified by monitoring the neck radius over time. Four primary regimes are identified, each characterized by qualitatively different interfacial behaviour. For shear-thinning and weakly shear-thickening fluids at small to moderate values of \mathcal{J} (i.e., $\mathcal{J} \lesssim 0.45$), the breakup follows the well-known end-pinching mechanism, where a droplet detaches from the tip of the retracting ligament. The regime map reveals that end-pinching escape persists across two rheological limits, shear-thickening (viscous) and shear-thinning (inertial).

In the intermediate range $0.06 \lesssim \mathcal{J} \lesssim 0.45$, we identify a no-neck regime, where the neck collapses monotonically or remains undeveloped due to the presence of extensive unyielded plugs (see figure 6), reaching neither breakup nor escape. Finally, for $\mathcal{J} \gtrsim 0.45$, a motionless regime emerges in which retraction is entirely suppressed by yield stress (e.g., yield stresses dominate over the viscous and inertial contributions). These last two regimes, are largely insensitive to variations in the flow-behaviour index n because the dominant balance is controlled by the yield stress rather than the shear-dependent viscosity.

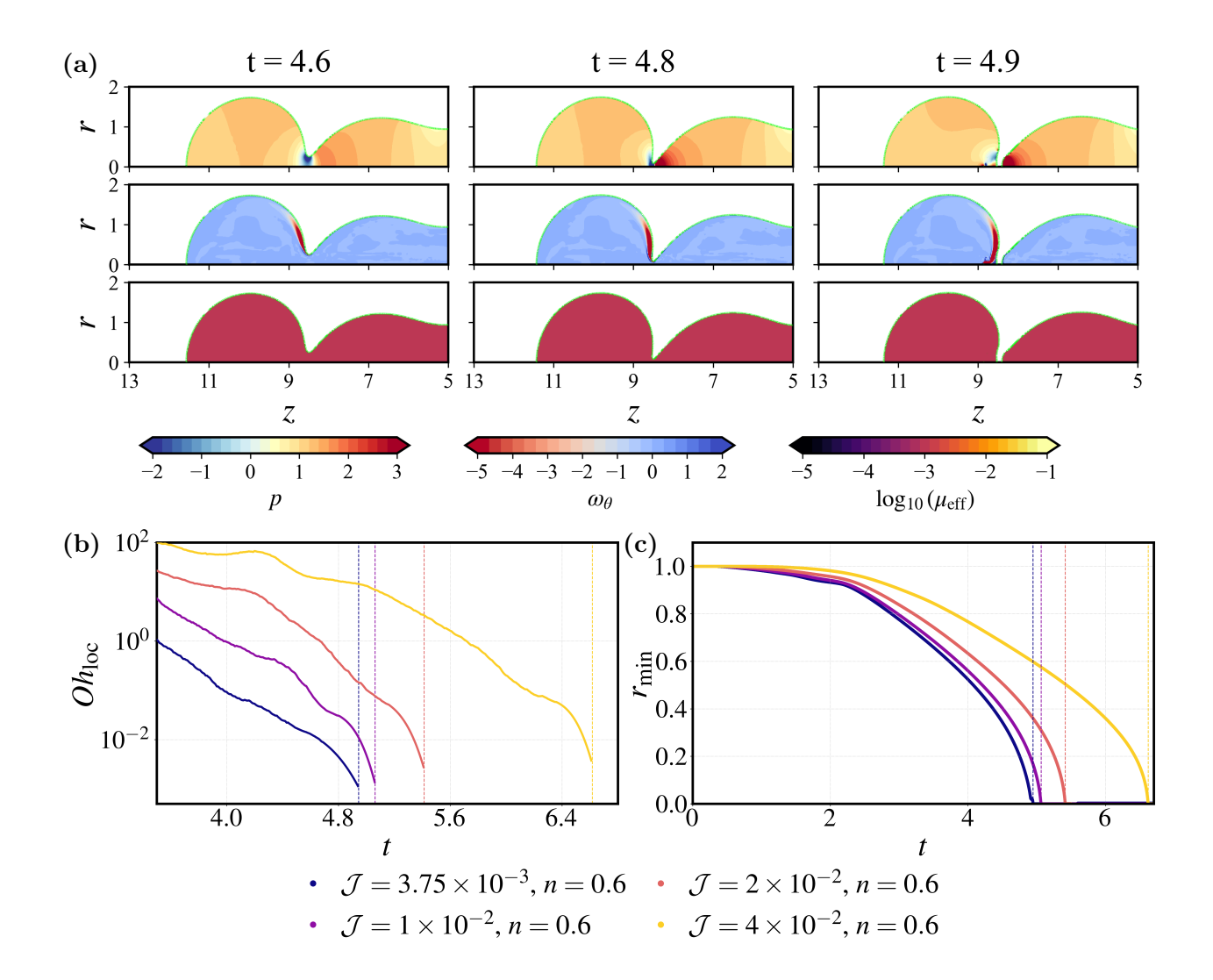


FIG. 3: End-pinching regime. (a) Temporal sequence of the pressure field p (top), azimuthal vorticity ω_{θ} (middle), and effective viscosity $\log_{10}(\mu_{\text{eff}})$ (bottom) during the final stages of breakup, shown at t=4.6, 4.8, and 4.9 for $Oh_K=0.001$ and $\mathcal{J}=0$ and n=1 (b) Temporal evolution of the local Ohnesorge number Oh_{loc} at the neck. (c) Normalized minimum radius r_{min} versus time for several \mathcal{J} at fixed n=0.6

B. Pinch-off regime

Figure 3a shows the time evolution in time of the shape of a Newtonian ligament with $Oh_K = 0.001$. For this set of parameters, the temporal evolution of the ligament is governed by the interplay between capillary, viscous, and inertial forces. Since the simulation starts from a motionless ligament, there is a pressure difference inside the ligament as the pressure at the hemispherical tip is twice that in the cylindrical ligament.

This pressure gradient drives fluid from the tip to the ligament, as the flow encounters viscosity resistance it results in the formation of a bulbous structure edge at tip, and subsequently it leads to the formation of a neck. As the bulbous structure grows, the neck size decreases in time approaching a capillary singularity. The corresponding radial scaling extracted from our simulations (see Appendix) shows excellent agreement with the classical inertial—capillary similarity law $r_{\min} \propto (t_b - t)^{2/3}$, where r_{\min} represents the neck radius and t_b is the breakup time [23]. At the moment of breakup, a large capillary pressure is confined within the thinning neck, while a thin azimuthal vorticity layer develops only in the immediate vicinity of the neck region (see top and middle panels of figure 3a).

As shown in figure 2, the pinch-off regime extends for shear-thinning threads up to values of $\mathcal{J} \lesssim 0.05$. In shear-thinning fluids, the apparent viscosity decreases with increasing local shear rate, $\mu_{\text{eff}} \sim \dot{\gamma}^{n-1}$ with n < 1. During necking, large velocity gradients develop in the thinning region due to the interfacial shape, lowering the μ_{eff} and therefore the viscous resistance to the capillary forces. This drives the local Ohnesorge number to values $Oh_{\text{loc}} \ll 10^{-2}$, at which point the thinning dynamics become effectively inertial-capillary and insensitive to the yield stress. Figures 3b-c show that increasing \mathcal{J} merely delays the onset of this regime; in all cases Oh_{loc} eventually falls below 10^{-2} , after which the neck follows the classical inertial-capillary similarity and complete pinch-off.

C. Escape from pinch-off regime

For shear-thickening fluids, we observe a reopening of the neck without the formation of a capillary singularity for $\mathcal{J} \lesssim 0.06$. This behaviour follows directly from the increase of the apparent viscosity with the shear rate, $\mu_{\text{eff}} \sim \dot{\gamma}^{n-1}$ with n > 1. As the neck thins, the local strain rate rises sharply, causing μ_{eff} and the associated viscous stresses to grow sharply. The enhanced viscous resistance counteracts the capillary-driven collapse and redistributes momentum away from the neck, progressively decelerating the thinning. Once the viscous stresses dominate capillarity, the axial flow reverses and the neck reopens, thereby preventing the onset of a singularity even at relatively small plastocapillary numbers. This enhanced viscous resistance effectively pushes fluid from the neck toward the bulbous structure ends, promoting a reopening of the neck, a mechanism observed in viscous Newtonian threads [13].

The dynamics leading to reopening are illustrated in figure 4 by plotting the azimuthal

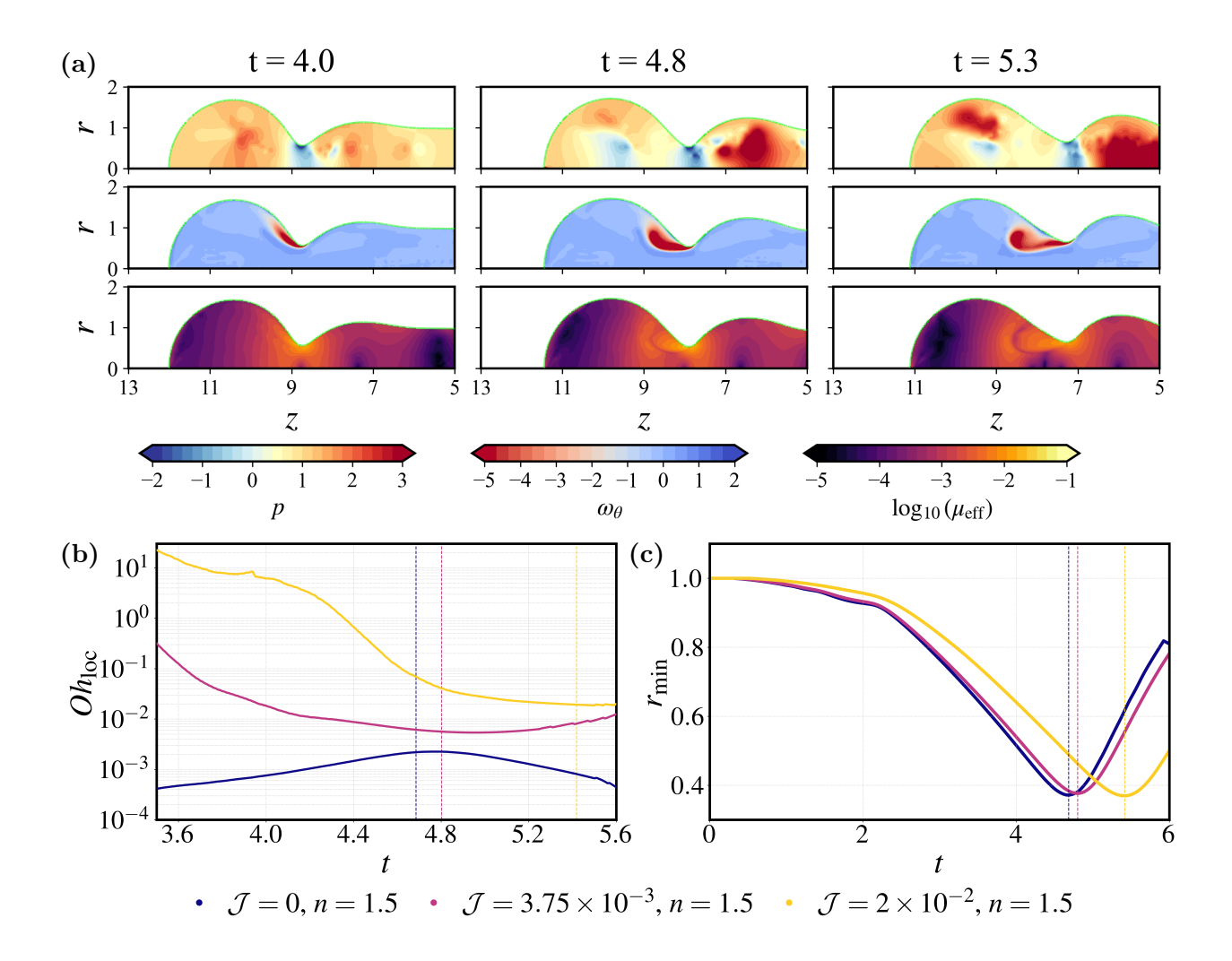


FIG. 4: Shear thickening reopening regime. (a) Snapshots of pressure p, azimuthal vorticity ω_{θ} , and $\log_{10}(\mu_{\text{eff}})$ for the case $Oh_K = 0.001$, $\mathcal{J} = 0$, and n = 1.5, with each row showing one of the three fields at times t = 4.0, 4.8, and 5.3 from left to right. (b) Temporal evolution of the local Ohnesorge number Oh_{loc} at the neck. (c) Normalized minimum radius r_{min} versus time for several \mathcal{J} at fixed n = 1.5

vorticity, pressure, and apparent viscosity fields. At early times, only weak azimuthal vorticity is generated near the neck, resembling the Newtonian case (t = 4). As thinning proceeds, large axial velocity gradients produce a strong concentration of azimuthal vorticity on the bulk side of the neck, forming a thin interfacial layer in which both the shear rate and μ_{eff} vary sharply. As time advances, a higher regeneration of azimuthal vorticity is observed that draws fluid from the neck towards the tip marking the onset of the escape process. After reversal, viscous diffusion transports azimuthal vorticity into the edge tip and thickens

the interfacial shear layer, leading to the expansion of the vortex ring characteristic of the relaxation stage.

The interplay between $Oh_{\rm loc}$, \mathcal{J} and the evolution of the neck $(r_{\rm min})$ clarifies the mechanisms governing reopening in shear-thickening ligaments. Across all cases, the neck thins to nearly the same minimum radius $r_{\rm min} \approx 0.4$, indicating that shear thinning behaviour, rather than the yield stress, is responsible for reopening. The main effect of increasing \mathcal{J} is instead to delay the onset of rapid thinning, for larger \mathcal{J} the neck remains larger for longer because the yield stress resists deformation, keeping both the local strain rate and the effective viscosity small during the early stages. Once the capillary pressure exceeds the yield threshold, the neck begins to deform more rapidly and the strain rate increases abruptly. This increase in $\dot{\gamma}$ produces a larger effective viscosity $\mu_{\rm eff}$, which leads to a higher $Oh_{\rm loc}$ in the $\mathcal{J}=0.02$ case despite the similar value of $r_{\rm min}$. The trends in figure 4b therefore reflect the stronger growth of $\mu_{\rm eff}$ during the late-stage thinning for larger \mathcal{J} , rather than any geometric differences. As shown in figure 4a, this enhanced viscosity is accompanied by the development of a thin, high-shear interfacial layer and a localized flow reversal, which ultimately drives the reopening of the neck.

Next we examine the behaviour of shear-thinning fluids. A natural expectation is that Newtonian ligaments at low Oh_K (effectively inviscid) and shear-thinning fluids at low n (which exhibit even weaker local viscous damping) should undergo pinch-off. Unexpectedly, we find that sufficiently strong shear-thinning at small \mathcal{J} ($n \lesssim 0.6, \mathcal{J} \lesssim 3.5 \times 10^{-3}$) can instead lead to reopening (see figure 5). In this regime, the apparent viscosity decreases dramatically with shear rate, resulting in a very small local Ohnesorge number $(Oh_{loc} \ll 1)$, eliminating viscous diffusion near the interface. As a consequence, the azimuthal vorticity sheet generated during the early stages of necking cannot remain attached to the interface. It is instead advected away by inertia and rolls up into a coherent vortex ring on the bulk side of the neck (see figure 5). The subsequent neck reopening is therefore not viscously driven but arises from an inertial-capillary rebound: once viscous damping vanishes, rapid pressure redistribution and inertial overshoot decelerate the collapse and push the interface outward, restoring the ligament shape. The detached vortices observed downstream correspond to the rolled-up remnants of the interfacial shear layer, which are convected into the bulk without diffusive decay. This represents a distinct, inertia-dominated route to pinch-off escape induced by extreme shear-thinning rheology.

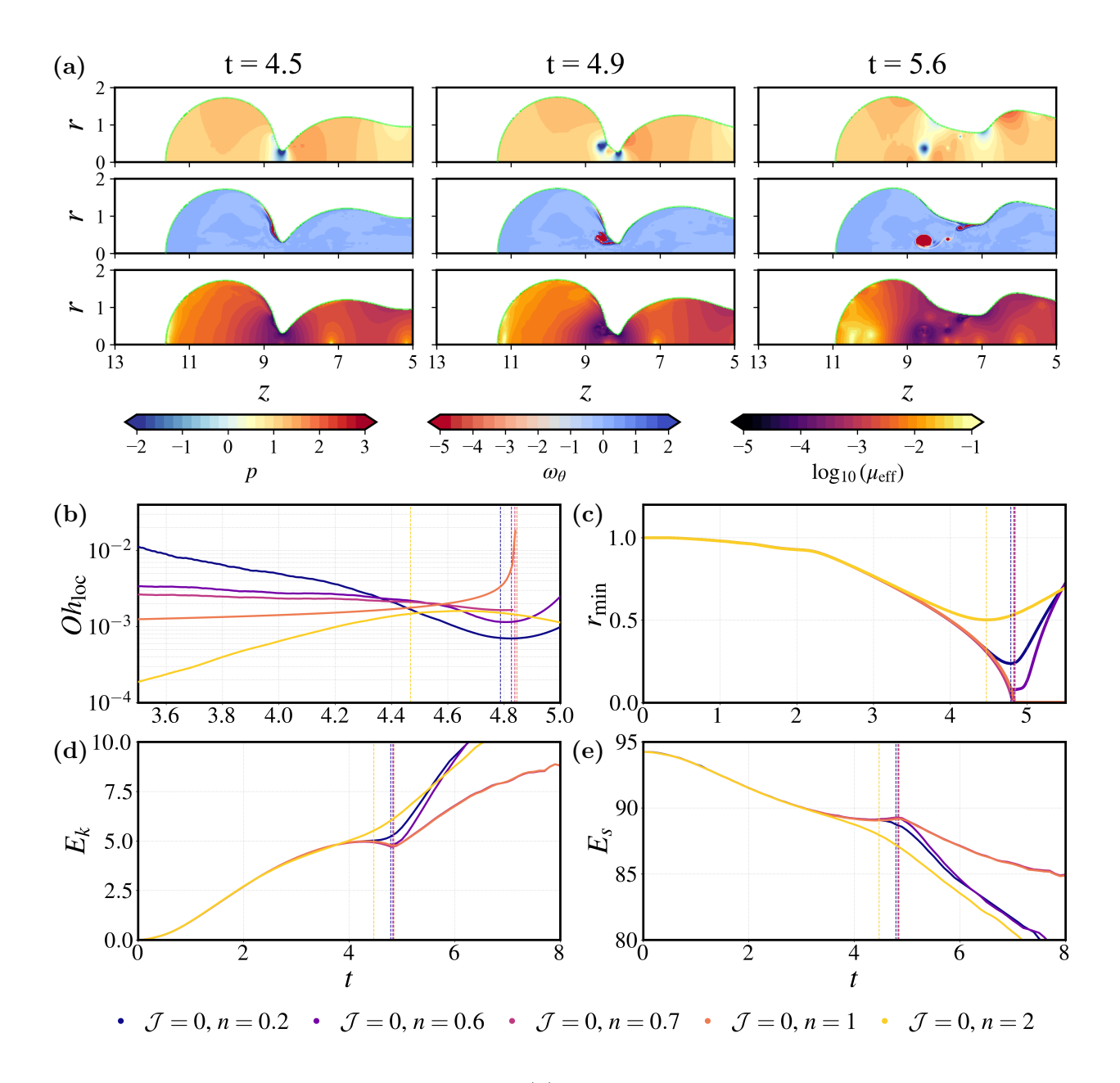


FIG. 5: Shear-thinning reopening regime. (a) Snapshots of pressure p, azimuthal vorticity ω_{θ} , and $\log_{10}(\mu_{\text{eff}})$ for the case $Oh_K = 0.001$, $\mathcal{J} = 0$, and n = 0.2, with each row showing one of the three fields at times t = 4.5, 4.9, and 5.6 from left to right. (b) Temporal evolution of the local Ohnesorge number Oh_{loc} . (c) Minimum neck radius r_{min} over time for several n at fixed $\mathcal{J} = 0$ (d) Temporal evolution of the total kinetic energy E_k . (e) Temporal evolution of the surface energy E_s

Figure 5d-e show the energy signature of the escape by plotting the temporal evolution of the kinetic energy E_k , and surface energy E_s for different n at $\mathcal{J} = 0$. Surface energy and kinetic energy are calculated as $E_s = \sigma \int_{\Gamma} 2\pi r \, dl$ and $E_k = 2\pi \iint_F \frac{1}{2}\rho |\mathbf{u}|^2 r \, dr dz$ where Γ is interface curve, dl is interface arc length element, r and z are cylindrical coordinates. These quantities reveal how the interplay between capillary, viscous, and inertial effects governs the thinning and reopening of the ligament.

For shear-thinning and Newtonian cases ($n=0.2,\ 0.6,\$ and 1), the neck undergoes a rapid collapse followed by a rebound. Around the breakup time ($t\approx4.5$ –5), both E_k and E_s exhibit inflection points, coinciding with the minimum in r_{\min} . For the two cases that reopen (n=0.2 and 0.6), E_k continues to grow slightly faster after the neck minimum, reflecting an inertial surge that drives the rebound and vortex-ring formation observed in the azimuthal vorticity fields. Shortly thereafter, E_s partially recovers, meaning a reconversion of kinetic to interfacial energy as the ligament expands. This non-monotonic, reversible exchange between E_k and E_s is a hallmark of an underdamped inertia-capillary system, where viscosity is too weak to dissipate the energy released by surface-tension collapse. By contrast, for shear-thickening fluids (n=2), E_k increases smoothly without a marked inflection, while E_s decreases monotonically. The energy transfer remains one-way: surface energy is converted into kinetic energy and subsequently dissipated through viscous stresses rather than reconverted into interfacial motion. The comparison across n thus underscores the rheological control of the energy budget: decreasing n enhances inertial storage and rebound, while increasing n amplifies viscous dissipation and flow stabilisation.

Our observations can be interpreted within the framework proposed by Wee et al. [24], who identified two distinct routes for escaping pinch-off in low-viscosity Newtonian sheets. At asymptotically small Ohnesorge numbers $(Oh \to 0)$, the dynamics is governed by a local balance between viscous and capillary stresses, forming a 'viscous-resistance' regime in which even minute viscosity becomes dynamically relevant once the neck is sufficiently small. At slightly larger, yet still small, Oh, the escape instead arises from 'vorticity generation' along the free surface as viscous stresses generates vorticity that results in the reopening of the neck. The present Herschel–Bulkley results extend this picture to non-Newtonian rheology by introducing a dynamically evolving local Ohnesorge number, Oh_{loc} , through the shearrate dependence of μ_{eff} . In shear-thickening cases, the rapid increase of μ_{eff} raises Oh_{loc} and promotes a viscous, vorticity-driven reopening, analogous to Wee et al. [24]. In contrast, for

strongly shear-thinning threads, $\mu_{\rm eff}$ decreases sharply under large shear, driving $Oh_{\rm loc} \ll 1$ and suppressing viscous diffusion. In this limit, the interfacial shear layer detaches and rolls up into a vortex ring, and the neck reopens through an inertial-capillary rebound rather than viscous resistance. Thus, our results generalize the two escape pathways of Wee *et al.* [24] to non-Newtonian fluids, revealing a rheology-dependent transition between viscous and inertial reopening mechanisms.

Vorticity generation near interfaces – The differences in neck dynamics and reopening behaviour between shear-thickening and shear-thinning ligaments can be interpreted through the generation and transport of vorticity in the neck region; this is consistent with the work of Batchelor [25] who concluded that vorticity in a homogeneous fluid is generated at the boundaries only. We can assume that the interface behaves as a viscous free-surface because of the vanishing viscosity and density ratios, as in previous work by Kamat et al. [15], Longuet-Higgins [26], Cresswell and Morton [27], Peck and Sigurdson [28], Lundgren and Koumoutsakos [29], Brøns et al. [30], Thoraval et al. [31], Constante-Amores et al. [32]. For a Herschel–Bulkley fluid, the vorticity balance over a material volume $\mathcal{V}(t)$ is written as

$$\frac{D}{Dt} \int_{\mathcal{V}(t)} \boldsymbol{\omega} \, d\mathcal{V} = \underbrace{\int_{\mathcal{V}(t)} (\boldsymbol{\omega} \cdot \nabla) \boldsymbol{u} \, d\mathcal{V}}_{\text{vorticity stretching}} + \underbrace{\int_{\mathcal{V}(t)} \nabla \times \left(\frac{\nabla \cdot \boldsymbol{\tau}}{\rho}\right) d\mathcal{V}}_{\text{bulk HB stress}} + \underbrace{\int_{S(t)} 2 \, Oh_K \left[\mathbf{e}_{\theta}(\mathbf{n} \cdot \nabla) \frac{\partial u_n}{\partial s} - \kappa_t u_t\right] dS}_{\text{surface HB contribution}} \tag{4}$$

The first term in (4) describes vorticity stretching due to velocity gradients, the second accounts for bulk vorticity generation from spatial variations of the HB stress, and the third represents the vorticity flux produced by tangential stress along the free surface, where $u_n = \mathbf{n} \cdot \mathbf{u}$ and $u_t = \mathbf{t} \cdot \mathbf{u}$ are the normal and tangential velocity components.

The surface term shows explicitly that the rate of vorticity generation scales with Oh_K . For shear-thickening fluids (n > 1), the effective viscosity $\mu_{\text{eff}} \sim K\dot{\gamma}^{n-1}$ and hence Oh_K increase rapidly with local shear rate, amplifying the viscous generation at the interface. This produces a strong, attached vorticity layer on the bulk side of the neck and drives a recirculating back-flow that refills the neck, leading to viscous reopening. In contrast, for shear-thinning fluids (n < 1), Oh_K decreases under large shear, weakening the surface torque and reducing the bulk vorticity source. The resulting vorticity layer detaches and

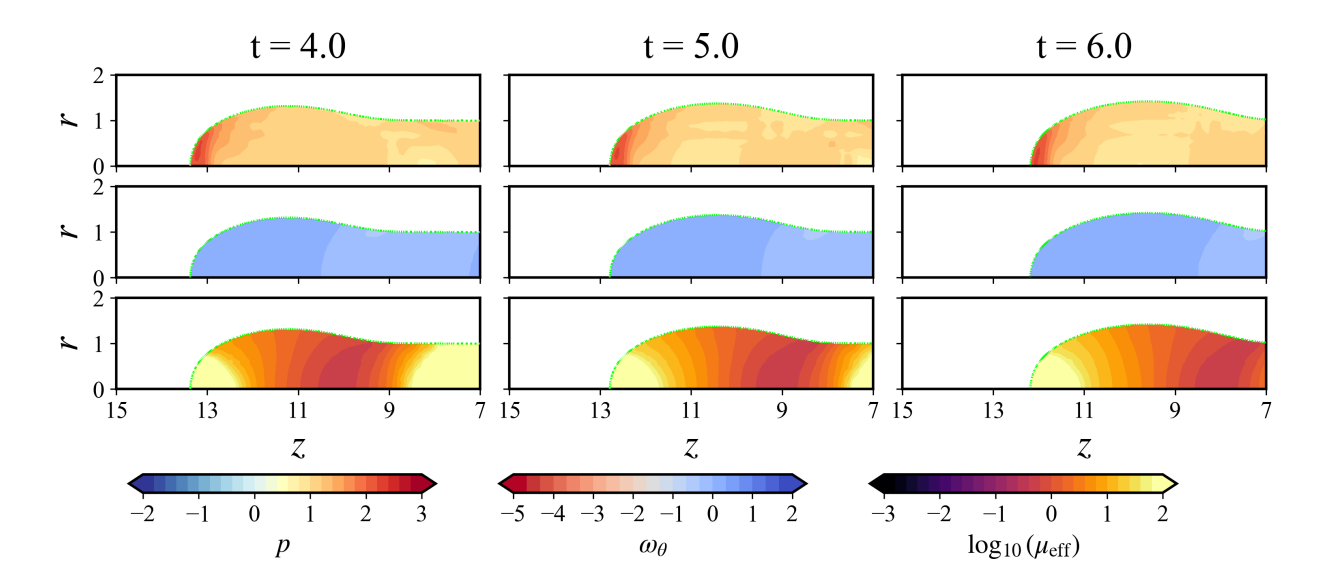


FIG. 6: No neck formation regime. Snapshots of pressure p, azimuthal vorticity ω_{θ} , and $\log_{10}(\mu_{\text{eff}})$ for the case $Oh_K = 0.001$, $\mathcal{J} = 0.3$, and n = 1, with each row showing one of the three fields at times t = 2.0, 4.0, and 8.0 from left to right.

rolls up into a vortex ring that convects downstream, preventing refilling and producing an inertial—capillary rebound instead.

To assess whether vorticity can influence the interfacial singularity, we compare the vorticity-diffusion time across the neck, $t_w = \rho r_{\min}^2/\mu_{\text{eff}}$, with the local inertial–capillary time, $t_{ic} = (\rho r_{\min}^3/\sigma)^{1/2}$; their ratio reduces to $t_w/t_{ic} = 1/Oh_{\text{loc}}$. Equivalently, the vorticity boundary-layer thickness over t_{ic} satisfies $\delta_{\omega}/r_{\min} \sim Oh_{\text{loc}}^{1/2}$. Hence, $Oh_{\text{loc}} \ll 1$, the thin attached shear layer of vorticity in the neck is advected into the neck faster than it diffuses, indicating an inertial–advective mechanism rather than diffusion-controlled escape. This reconciles our observations once a local, time-dependent Ohnesorge number is used in place of a fixed global value. When diffusion becomes negligible, this layer detaches and rolls up into a toroidal vortex ring on the bulk side. The process is Kelvin–Helmholtz–like in morphology—reflecting inviscid shear-layer roll-up—rather than a true KH instability sustained by a continuous velocity discontinuity

D. No neck regime

The lower boundary separating the pinch-off and smooth-retraction regimes arises when the yielded envelope around the neck no longer spans the axial extent of the necked region. To quantify this, we examined the interface profiles from the DNS at the onset of necking. At this stage the ligament is not deformed, thus the minimum radius remains close to $r_{\rm min}/R_0 \approx 1$, while the region over which the interface curvature departs from its far-field value extends axially over $L_z/R \simeq 2$ –3. These values are obtained directly from the simulated profiles and indicate that the capillary disturbance is confined to a few radii near the neck centre. Similar aspect ratios have been reported in earlier analyses of slender threads Stone and Leal [33].

Capillary forcing at the neck generates an interfacial stress of order $\tau(a) \sim \sigma/a$. In axisymmetric creeping flow, the disturbance stress decays approximately as $\tau(r) \sim \tau(a) \left(\frac{a}{r}\right)^2$, which follows from the 1/r velocity and $1/r^2$ stress fields of the Stokes equations. The outer radius of the yielded annulus, defined by $\tau(r_y) = \tau_y$, is therefore $r_y \sim \left(\frac{\sigma a}{\tau_y}\right)^{1/2}$. Pinch-off requires the neck to be fully yielded along its axial extent; once the yield envelope fails to reach the ligament ends $(r_y \lesssim L_z)$, the neck remains partially unyielded and can no longer localise. Setting $r_y \simeq L_z$ gives a threshold $\tau_y \sim \sigma a/L_z^2$, and subsequently $\mathcal{J}_c \equiv \tau_y R/2\sigma \sim aR_0/2L_z^2$, which defines the onset of the "no-neck" regime. Substituting the measured aspect ratios $(a_{\min}/R_0 \approx 1, L_z/R_0 \approx 2-3)$ yields $\mathcal{J} \approx 0.04$ –0.07, in close agreement with the numerically observed transition near $\mathcal{J} \simeq 0.05$ shown in figure 2. The result contains no adjustable parameters and follows directly from the measured neck geometry and the stress decay implied by the Stokes equations. Physically, the ends of the ligament, where curvature and capillary stress are largest, remain yielded and retract, while the central neck is shielded by an unyielded core that prevents further localisation and breakup.

E. Motionless regime

For sufficiently large \mathcal{J} the ligament does not move (see figure 7). The boundary separating motionless ligaments from the moving one arises from a simple capillary-yield balance. The associated capillary pressure at the tip of the ligament is $2\sigma/R_0$ while it is σ/R_0 at the ligament centre. Capillary motion can proceed only if the local pressure difference exceeds the material yield stress τ_y . When the minimum available capillary stress at the centre, $\Delta p_{\sigma} \simeq \sigma/R$, falls below τ_y , the surrounding material remains unyielded and the ligament becomes effectively frozen. Normalising stresses by the end-cap value $2\sigma/R_0$ defines the dimensionless plastocapillary number $\mathcal{J} = \tau_y R_0/(2\sigma)$, for which the condition $\tau_y \simeq \sigma/R$

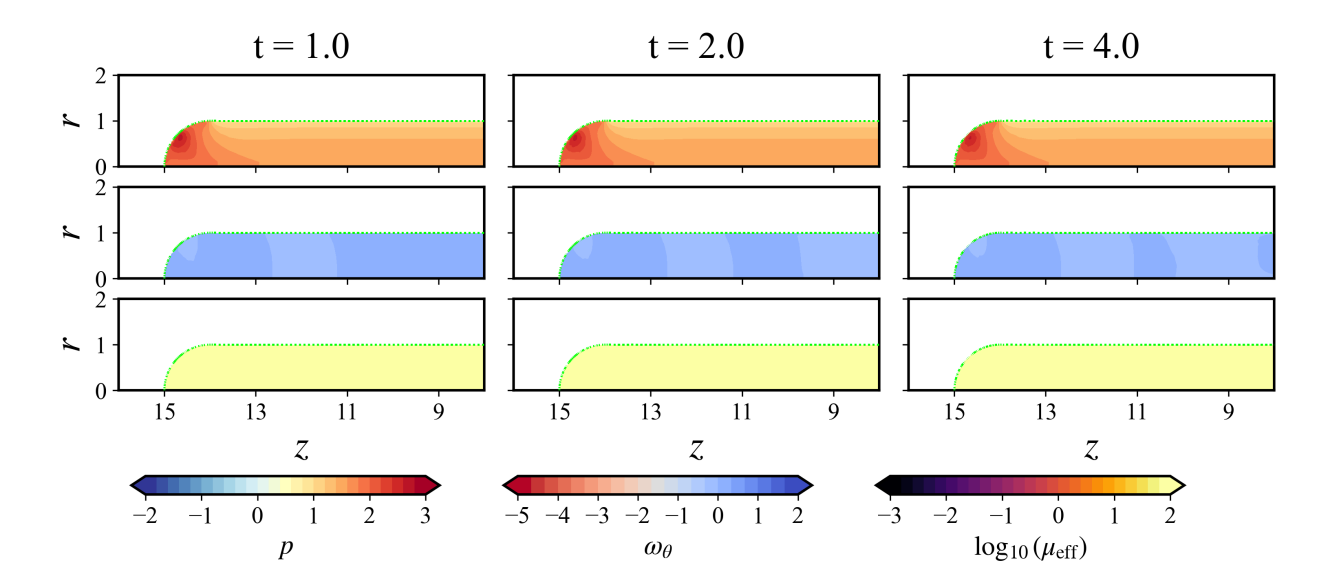


FIG. 7: Motionless regime. Snapshots of pressure p, azimuthal vorticity ω_{θ} , and $\log_{10}(\mu_{\text{eff}})$ for the case $Oh_K = 0.001$, $\mathcal{J} = 1.0$, and n = 1.0, with each row showing one of the three fields at times t = 1.0, 2.0, and 4.0 from left to right.

corresponds to a critical value $\mathcal{J}_{\text{crit}} \simeq 0.5$. Hence, ligaments with $\mathcal{J} \geq 0.5$ cannot generate sufficient interfacial pressure to overcome the yield resistance of the surrounding medium and remain motionless. Since this criterion involves only stresses and not strain rates, the flow-behaviour index n, plays no role in setting the arrest threshold. This vertical boundary in the (\mathcal{J}, n) plane is therefore fully determined by geometric curvature asymmetry and is independent of the rheological index n. This agrees well with the predictions of the simulations

IV. CONCLUSIONS

Capillary retraction of a Herschel-Bulkley ligament reveals a rich interplay between surface tension, yield stress, and inertia. Direct numerical simulations using the adaptive Volume-of-Fluid solver BASILISK show that deviations from Newtonian behaviour give rise to four distinct dynamical outcomes: inertial pinch-off, viscous (vorticity-driven) escape, inertial (rebound) escape, and arrested motion. These regimes organize systematically in the (n, \mathcal{J}) parameter space, where n is the flow-behaviour index and \mathcal{J} the plastocapillary number. Their boundaries are governed by the evolution of the local Ohnesorge number, which quantifies the instantaneous balance between viscous diffusion and inertial-capillary

collapse. When $Oh_{loc} \gtrsim O(1)$, viscous diffusion sustains an attached vorticity layer that drives a back-flow and a vorticity-driven escape. Conversely, when $Oh_{loc} \ll 1$, the vorticity sheet detaches and rolls into a toroidal vortex ring, producing an inertial rebound of the neck. This framework generalizes the Newtonian results of Hoepffner and Paré [13] and Wee et al. [24] to Herschel-Bulkley rheology. Finally, when the yield stress is sufficiently large, both mechanisms are suppressed and no neck forms; for sufficiently high yield stress, the ligament becomes completely immobilised as the yield resistance overcomes the capillary driving forces.

Most yield-stress fluids encountered experimentally, such as Carbopol gels or polymeric suspensions, exhibit measurable viscoelasticity in addition to their plastic response [34]. The present study isolates the purely viscoplastic limit through the Herschel–Bulkley formulation, thereby clarifying the individual roles of yield stress and shear-dependent viscosity in shaping end-pinching escape. While this simplification provides a useful theoretical baseline, the resulting dynamics cannot be mapped directly onto real yield-stress materials. Future work should therefore examine how elastic stress storage and relaxation modify the vorticity-driven and inertial-rebound pathways identified here.

Declaration of Interests. The authors report no conflict of interest.

Acknowledgments

This research used the Delta advanced computing and data resource which is supported by the National Science Foundation (award OAC 2005572) and the State of Illinois.

^[1] R. M. S. M. Schulkes, J. Fluid Mech. **309**, 277 (1996).

^[2] C. R. Anthony, H. Wee, V. Garg, S. S. Thete, P. M. Kamat, B. W. Wagoner, E. D. Wilkes, P. K. Notz, A. U. Chen, R. Suryo, et al., Annu. Rev. Fluid Mech. 55, 707 (2023).

^[3] D. Lohse, Annu. Rev. Fluid Mech. **54**, 349 (2022).

^[4] P. Shah, Y. Kevrekidis, and J. Benziger, Langmuir **15**, 1584 (1999).

^[5] J. Eggers and E. Villermaux, Rep. Prog. Phys. **71**, 036601 (2008).

^[6] S. D. Hoath, S. Jung, and I. M. Hutchings, Phys. Fluids 25, 021701 (2013).

- [7] C. R. Anthony, P. M. Kamat, M. T. Harris, and O. A. Basaran, Phys. Rev. Fluids 4, 093601 (2019).
- [8] C. Planchette, F. Marangon, W.-K. Hsiao, and G. Brenn, Phys. Rev. Fluids 4, 124004 (2019).
- [9] M. Schena, R. A. Heller, T. P. Theriault, K. Konrad, E. Lachenmeier, and R. W. Davis, Trends Biotechnol. 16, 301 (1998).
- [10] O. A. Basaran, AIChE J. 48, 1842 (2002).
- [11] A. Altieri, S. A. Cryer, and L. Acharya, Atomization Sprays 24, 695 (2014).
- [12] P. K. Notz and O. A. Basaran, J. Fluid Mech. **512**, 223 (2004).
- [13] J. Hoepffner and G. Paré, J. Fluid Mech. **734**, 183 (2013).
- [14] C. R. Constante-Amores, L. Kahouadji, A. Batchvarov, S. Shin, J. Chergui, D. Juric, and O. K. Matar, Phys. Rev. Fluids 5, 084007 (2020).
- [15] P. M. Kamat, B. W. Wagoner, A. A. Castrejón-Pita, J. R. Castrejón-Pita, C. R. Anthony, and O. A. Basaran, J. Fluid Mech. 899, A28 (2020).
- [16] M. De Corato, D. Tammaro, P. L. Maffettone, and N. Fueyo, J. Fluid Mech. 942, A55 (2022).
- [17] B. Keshavarz, V. Sharma, E. C. Houze, M. R. Koerner, J. R. Moore, P. M. Cotts, P. Threlfall-Holmes, and G. H. McKinley, J. Non-Newtonian Fluid Mech. 222, 171 (2015).
- [18] H. Deka, J.-L. Pierson, and E. J. Soares, J. Non-Newtonian Fluid Mech. 272, 104172 (2019).
- [19] S. Popinet, J. Comput. Phys. **228**, 5838 (2009).
- [20] S. Popinet et al., Basilisk, http://basilisk.fr (2013-2025).
- [21] J. A. Van Hooft, S. Popinet, C. C. Van Heerwaarden, S. J. A. Van Der Linden, S. R. De Roode, and B. J. H. Van De Wiel, Boundary-Layer Meteorol. 167, 421 (2018).
- [22] S. Yang, K. Zinelis, S. Chakraborty, and C. R. Constante-Amores, Pinch-off dynamics for a Newtonian liquid thread draining in a viscoplastic medium (2025), arXiv:2509.15046 [physics.flu-dyn].
- [23] R. F. Day, E. J. Hinch, and J. R. Lister, Phys. Rev. Lett. 80, 704 (1998).
- [24] H. Wee, A. H. Kumar, X. Liu, and O. A. Basaran, Phys. Rev. Fluids 9, 103601 (2024).
- [25] G. K. Batchelor, An Introduction to Fluid Dynamics, Cambridge Mathematical Library (Cambridge University Press, 1967).
- [26] M. S. Longuet-Higgins, J. Fluid Mech. **240**, 659–679 (1992).
- [27] R. W. Cresswell and B. R. Morton, Phys. Fluids 7, 1363 (1995).
- [28] B. Peck and L. Sigurdson, IMA J. Appl. Math. **61**, 1 (1998).

- [29] T. Lundgren and P. Koumoutsakos, J. Fluid Mech. 382, 351–366 (1999).
- [30] M. Brøns, M. C. Thompson, T. Leweke, and K. Hourigan, J. Fluid Mech. **758**, 63–93 (2014).
- [31] M.-J. Thoraval, Y. Li, and S. T. Thoroddsen, Phys. Rev. E 93, 033128 (2016).
- [32] C. R. Constante-Amores, A. Batchvarov, L. Kahouadji, S. Shin, J. Chergui, D. Juric, and O. Matar, J. Fluid Mech. 925, A15 (2021).
- [33] H. A. Stone and L. G. Leal, J. Fluid Mech. 198, 399 (1989).
- [34] M. T. Hossain, W. Eom, A. Shah, A. Lowe, D. Fudge, S. H. Tawfick, and R. H. Ewoldt, J. Non-Newtonian Fluid Mech., 105440 (2025).

APPENDICES

Sensitivity to the regularization parameter ε in the Herschel–Bulkley formulation

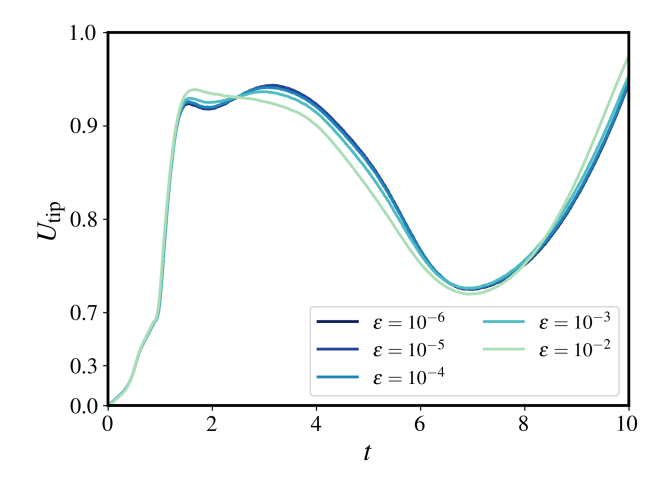


FIG. 8: Epsilon independence check at $L_0 = 15, Oh_K = 0.005, J = 0.05, n = 2$ following ligament tip speed U_{tip}

The Herschel-Bulkley model is implemented using a regularized formulation in which the apparent viscosity is smoothed through an ε -dependent function to prevent singularities as the strain-rate magnitude $||\mathcal{D}|| \to 0$. Consequently, the yield surface cannot be sharply captured, since $||\mathcal{D}||$ remains finite for any $\varepsilon > 0$. Figure 8 examines the influence of the regularization parameter ε with respect to the tip velocity U_{tip} over time for a retracting ligament of $Oh_K = 0.005$, J = 0.05, n = 2 by varying ε from $10^{-2} - 10^{-7}$. Similar behaviour is observed, but for $\varepsilon < 10^{-4}$, all the curves follow the same trend. This analysis results in choosing $\varepsilon = 10^{-4}$ for all simulations reported in this work. The influence of the regularization parameter ($\varepsilon = 1 \times 10^{-4}$), which is of the comparable magnitude to Deka *et al.* [18] (i.e., $\varepsilon = 1 \times 10^{-5}$).

For additional validation of the Herschel-Bulkley formulation, we refer the reader to Yang et al. [22], who analyzed the breakup dynamics of a Newtonian liquid thread surrounded by a viscoplastic medium. In their study, the temporal evolution of the neck radius for the Newtonian reference and the Herschel-Bulkley case with $\mathcal{J} = 0$ and n = 1 exhibited excellent agreement, recovering the expected Newtonian scaling laws. This outcome further substantiates the accuracy of the Herschel-Bulkley implementation employed here. Furthermore, Yang et al. [22] showed that the numerical approach faithfully captures the scaling

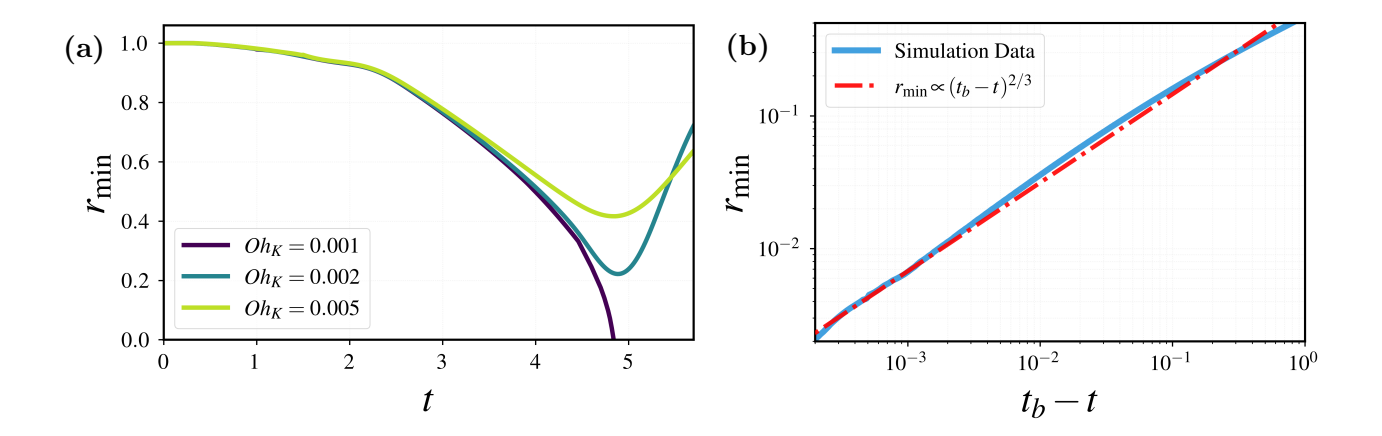


FIG. 9: (a) r_{\min} vs t for $Oh_K = 0.001$, 0.002, and 0.005 (b) r_{\min} vs $t_b - t$ for a Newtonian ligament at $Oh_K = 0.001$, demonstrating the inertial scaling $r_{\min} \propto (t_b - t)^{2/3}$

behaviour of both the neck radius and the peak axial velocity across shear-thinning and shear-thickening regimes.

Extra Newtonian simulations

To further characterize the dynamics of thread breakup in the Newtonian limit, we perform additional simulations varying the Ohnesorge number $Oh_K = 0.001$, 0.002, and 0.005. Figure 9 presents the temporal evolution of the normalized minimum radius r_{\min} as a function of the non-dimensional time.

All cases exhibit the classical stages of capillary-driven pinch-off. Initially, the neck thins gradually under the combined action of capillary suction and inertia, followed by a rapid acceleration as the neck approaches the singularity. The minimum radius decreases self-similarly, recovering the well-established Newtonian scaling $r_{\min} \propto (t_b - t)^{2/3}$ in the inertial regime. For lower Oh_K , viscous effects are negligible and the pinch-off proceeds faster, as shown by the earlier collapse of the blue and orange curves.

Overall, these Newtonian simulations establish a consistent reference for subsequent comparisons with viscoplastic cases, ensuring that the solver faithfully reproduces the expected inertio—capillary scaling behaviour and the characteristic suction-driven end-pinching mechanism.